



## Emplacement and tectonic deformation of smooth plains in the Caloris basin, Mercury

Thomas R. Watters<sup>a,\*</sup>, Scott L. Murchie<sup>b</sup>, Mark S. Robinson<sup>c</sup>, Sean C. Solomon<sup>d</sup>, Brett W. Denevi<sup>c</sup>, Sarah L. André<sup>a</sup>, James W. Head<sup>e</sup>

<sup>a</sup> Center for Earth and Planetary Studies, National Air and Space Museum, Smithsonian Institution, Washington, DC 20560, USA

<sup>b</sup> Johns Hopkins University Applied Physics Laboratory, Laurel, MD 20723, USA

<sup>c</sup> School of Earth and Space Exploration, Arizona State University, Tempe, AZ 85251, USA

<sup>d</sup> Department of Terrestrial Magnetism, Carnegie Institution of Washington, Washington, DC 20015, USA

<sup>e</sup> Department of Geological Sciences, Brown University, Providence, RI 02912, USA

### ARTICLE INFO

#### Article history:

Accepted 23 March 2009

Available online 5 May 2009

Editor: T. Spohn

#### Keywords:

Mercury

MESSENGER

Caloris basin

tectonics

geologic history

### ABSTRACT

MESSENGER's first flyby of Mercury provided the first complete view of the Caloris basin and its interior smooth plains. Multispectral imaging shows that the interior plains are spectrally distinct from surrounding terrain, with a reflectance about 15–20% higher and a steeper spectral slope than the global average. The Caloris basin rim massifs and hummocky material, in contrast, have lower reflectance and a shallower spectral slope than the global average and extend around the entire basin. Isolated, relatively red patches along the margins of Caloris each surround irregularly shaped, scalloped-edged, rimless depressions that are interpreted to be volcanic vents, some with associated pyroclastic deposits. A nearly continuous annulus of smooth plains exterior to the basin displays spectral characteristics that contrast sharply with those of the basin-interior smooth plains. The exterior smooth plains are lower in reflectance and spectrally similar to the Caloris rim massifs and the hummocky materials. The rims and floors of larger impact craters in the interior plains expose low-reflectance material. There is widespread evidence of contractional and extensional tectonic deformation of the Caloris interior smooth plains. A set of linear radial graben, Pantheon Fossae, radiates outward from a zone near the basin center, and some of these graben extend to and intersect a set of generally basin-concentric graben distributed along the outer margin of the Caloris basin floor. The average areal extensional strain expressed by the mapped system of graben is ~0.08%. Wrinkle ridges also deform the interior smooth plains and predate both basin-radial and basin-concentric graben. The average areal contractional strain expressed by the mapped wrinkle ridges is ~0.07%. The density of wrinkle ridges on the western interior smooth plains is less than on the eastern interior plains, in contrast to the more even distribution of graben. A similar difference is seen between the density of wrinkle ridges on the western and eastern exterior smooth plains, with far fewer wrinkle ridges per unit area on the western annular plains. Superposition relations, spectral contrast, and the occurrence of volcanic vents and possible pyroclastic deposits all support a volcanic origin for the Caloris interior plains. Crater counts indicate that the Caloris exterior plains and hummocky material are younger than the Caloris rim and interior plains and are therefore also likely volcanic in origin. The contrast in spectral properties between the interior and exterior plains indicates a difference in the composition of the two expanses of volcanic material. Models for extensional tectonic deformation of the Caloris basin interior inferred from the distribution of graben viewed by Mariner 10 must be reevaluated to account for the discovery of Pantheon Fossae.

Published by Elsevier B.V.

### 1. Introduction

Among the most important outcomes of the three Mariner 10 flybys of Mercury in 1974–1975 was discovery of the Caloris impact basin. Although less than half of the basin was imaged by Mariner 10, it was clearly recognized as one of the largest in the Solar System. The portion of the basin interior imaged by Mariner 10 is dominated by

smooth plains, which display wrinkle ridges and troughs interpreted to record multiple episodes of deformation (Strom et al., 1975; Melosh and McKinnon, 1988; Watters et al., 2005). Wrinkle ridges are common tectonic landforms typically found in plains material on the Moon and terrestrial planets (Strom, 1972; Bryan, 1973; Watters, 1988) and are interpreted to result from a combination of folding and thrust faulting (Plescia and Golombek, 1986; Watters, 1988; Schultz, 2000; Golombek et al., 2001; Watters, 2004). Within Caloris, wrinkle ridges fall within roughly arcuate regions near the basin margin and have orientations that are both concentric and radial to the basin

\* Corresponding author.

E-mail address: [watterst@si.edu](mailto:watterst@si.edu) (T.R. Watters).

center (Maxwell and Gifford, 1980; Melosh and McKinnon, 1988). The spatial distribution and pattern of wrinkle ridges in Caloris are broadly similar to those of wrinkle ridges in lunar maria (Strom, 1972; Bryan, 1973; Maxwell et al., 1975; Maxwell and Gifford, 1980; Solomon and Head, 1980).

A network of troughs in the portion of Caloris imaged by Mariner 10 displays a combination of linear and sinuous segments. These troughs are interpreted to be extensional tectonic landforms (Strom et al., 1975; Dzurisin, 1978; Melosh and McKinnon, 1988; Watters et al., 2005), the surface expression of antithetic normal faults forming graben. As with the wrinkle ridges, the graben have two dominant orientations, basin concentric and basin radial. The combination of basin-concentric and basin-radial graben forms a distinctly polygonal pattern (Dzurisin, 1978), with the maximum width of some polygons as great as ~50 km (Watters et al., 2005). Individual graben that form the polygons have widths from hundreds of meters to 10 km, depths of 100–200 m, and slopes on the bounding walls of <10° (Dzurisin, 1978; Watters et al., 2005; Watters and Nimmo, in press). The graben imaged by Mariner 10 are distributed in an arcuate zone ~180 to ~450 km from the basin's eastern rim, and they crosscut the wrinkle ridges, indicating that the graben are younger (Strom et al., 1975; Dzurisin, 1978; Melosh and McKinnon, 1988; Watters et al., 2005).

The geologic evolution of the Caloris basin may have been linked to that of material exterior to the basin rim. Two large-scale units in the exterior annulus imaged by Mariner 10 are hummocky material and smooth plains. The hummocky material consists of patches of rolling hills interpreted previously as Caloris impact ejecta (Guest and Greeley, 1983; Spudis and Guest, 1988). The smooth plains appear locally to embay and bury the hummocky material (Spudis and Guest, 1988) and constitute the most areally extensive unit in the Caloris exterior annulus. Broad expanses of smooth plains in Tir Planitia (~0°N, 180°E), Odin Planitia (~25°N, 190°E), and Suisei Planitia (~60°N, 200°E) make up the bulk of the eastern exterior annulus of circum-basin material viewed by Mariner 10. Wrinkle ridges are common in these basin-exterior smooth plains (Strom et al., 1975; Melosh and McKinnon, 1988; Spudis and Guest, 1988; Watters and Nimmo, in press), and their orientations led some workers to suggest a relationship between the Caloris basin and the stresses that produced the ridges (Strom et al., 1975; Melosh and McKinnon, 1988; Spudis and Guest, 1988). However, an analysis of the orientations of wrinkle ridges in the exterior smooth plains indicates that most ridges are neither strongly concentric nor predominantly radial to the basin (Watters and Nimmo, in press).

The origin of the smooth plains, both within the Caloris basin and in the exterior annulus, has not been readily resolvable from Mariner 10 observations. Spudis and Guest (1988) interpreted the general appearance of the undeformed portions of the interior smooth plains as evidence for a volcanic origin. Arguments cited for an impact-melt or ejecta origin for these smooth plains material included the lack of discernable volcanic features and the lack of albedo or color contrast between smooth plains and heavily cratered highlands (Wilhelms, 1976). Crater density measurements indicated that interior and exterior smooth plains are younger than the Caloris basin (Spudis and Guest, 1988), however, implying that neither unit can be Caloris ejecta.

The flyby of Mercury by the MErcury Surface, Space ENvironment, GEOchemistry, and Ranging (MESSENGER) spacecraft on 14 January 2008 (Solomon et al., 2008) provided the first complete view of the Caloris basin interior and exterior annulus. The Mercury Dual Imaging System (MDIS) (Hawkins et al., 2007), a co-articulated multispectral wide-angle camera (WAC) and monochromatic narrow-angle camera (NAC), obtained more than 1200 images of Mercury during the flyby. MDIS images were calibrated to radiance factor (or  $I/F$ , the observed radiance divided by solar irradiance) and photometrically corrected to standard viewing geometry (30° solar incidence and 0° emission angles) (Robinson et al., 2008).

Here we synthesize MESSENGER observations of the Caloris interior and exterior smooth plains to assess their origin, emplacement history, and subsequent tectonic deformation. WAC multi-spectral data were used to identify distinct spectral units in the Caloris basin materials and the interior and exterior smooth plains. From NAC image mosaics, we mapped the tectonic features that deform basin-interior and basin-exterior smooth plains in previously unseen areas. These observations, combined with previous mapping of structures in the portion of the basin imaged by Mariner 10, provide the most complete view of the spatial distribution of tectonic features in the Caloris basin to date. We discuss hypotheses for the origin and emplacement of the basin-interior and basin-exterior smooth plains in light of spectral data, morphology, and embayment and superposition relations, and we summarize proposed models for the tectonic stresses that deformed the interior and exterior smooth plains. Finally, we suggest a reconstruction of the principal stages in the volcanic and tectonic history of the Caloris basin.

## 2. Diameter of Caloris

The rim of the Caloris basin is composed of a series of rugged massifs as much as 50 km across (Guest and Greeley, 1983; Spudis and Guest, 1988). From the portion of the main rim imaged by Mariner 10, the basin's diameter was estimated to be between 1300 km (Strom et al., 1975) and 1420 km (Maxwell and Gifford, 1980). Initial circular fits to the complete Caloris rim from MESSENGER images yielded a main basin rim diameter of 1550 km (Murchie et al., 2008). Fassett et al. (2009–this issue) fit an ellipse to mapped occurrences of Caloris Montes massifs and inferred basin ring principal axis lengths of 1525 and 1315 km, with the major axis oriented east-northeast–west-northwest.

## 3. Spectral characteristics of the basin and exterior materials

### 3.1. Overview of spectral units

Spectral variations of Caloris interior and exterior smooth plains materials and other basin materials and deposits are shown in Fig. 1. The visible- and infrared-wavelength color composite (Fig. 1A) highlights differences in reflectance. Principal component (PC) analysis of the WAC 11-band color data and spectral ratios were used to identify and map spectral contrasts between materials interior and exterior to the Caloris basin (Murchie et al., 2008; Robinson et al., 2008). These derived parameters show variations in spectral slope at key wavelengths (Fig. 1B). Three areally extensive spectral terrain types have been identified: smooth plains (SP), spectrally intermediate terrain (IT), and low-reflectance material (LRM) (Robinson et al., 2008; Denevi et al., in press). The smooth plains can be further subdivided into high-reflectance red plains (HRP), intermediate plains (IP), and low-reflectance blue plains (LBP) (Denevi et al., in press). Although these units differ in reflectance, they share a red, lunar-like spectral slope indicative of mature, space-weathered soils. In addition, three other spatially restricted and spectrally distinct units were identified: fresh crater ejecta, bright crater-floor deposits, and moderately high-reflectance, relatively red material sometimes associated with rimless depressions (Robinson et al., 2008). All of these units are found in the vicinity of Caloris.

### 3.2. Basin and interior smooth plains materials

The interior of Caloris contains HRP material that is about 15–20% higher in reflectance than the global average (Fig. 1) and higher in reflectance than the rim massifs (Fig. 2A), exterior hummocky material (Fig. 2B), and exterior smooth plains (Fig. 2C). The interior plains also have a slightly steeper spectral slope, as measured by the ratio of reflectance at 750 nm to that at 430 nm, which is about 4%

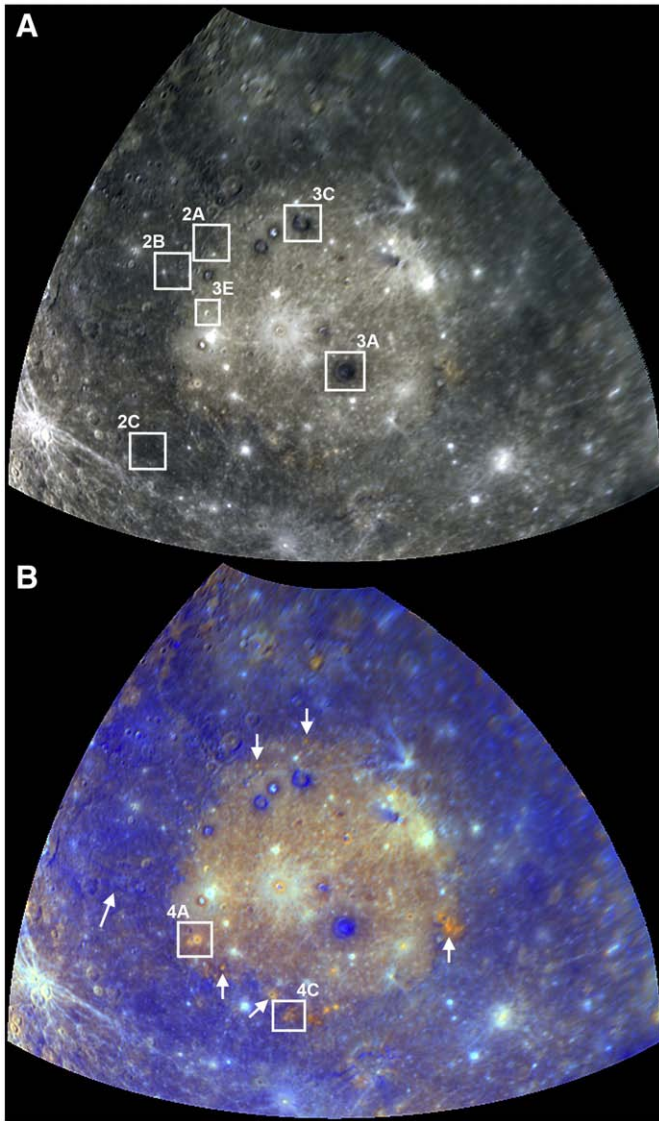


**Fig. 1.** The Caloris basin and exterior annulus. (A) WAC color composite with the 1000-, 750-, and 480-nm images in the red, green, and blue image planes, respectively. White boxes show the locations of unit type areas in Fig. 2 and impact craters in Fig. 3. (B) A color composite of the spectral parameters used to separate units. The first principal component (PC1) emphasizes variations in reflectance, and the second principal component (PC2) emphasizes spectral variations related to the physical state or chemistry of the material. The dominant variation represented by PC2 is slope of the spectral continuum. The inverse of PC2, PC1, and the 430-nm/560-nm reflectance ratio are shown in the red, green, and blue image planes, respectively. White boxes show the locations of volcanic features in Fig. 4. Short white arrows indicate the locations of diffuse red spots that can be associated with rimless, scallop-edged depressions. The long white arrow shows the location of a prominent linear streamer.

higher than that of the hummocky material (Murchie et al., 2008; Robinson et al., 2008). Rim massifs and hummocky material share similar spectral properties that include a normalized reflectance of  $\sim 0.085$  at 560 nm and a red, approximately lunar-like spectral slope (Murchie et al., 2008; Robinson et al., 2008). Similarities in the color and morphology indicate that the rim massifs of the eastern portion of the Caloris basin imaged by Mariner 10 extend around the entire basin (Fig. 1B).

Impact craters with diameters up to 100 km occur in the interior plains, and the larger craters can be divided into four groups on the basis of spectral characteristics of their rims and floors. Group A craters, most conspicuous in the center of the basin, exhibit floors and rims of LRM with a lower reflectance than both the interior plains and

exterior hummocky material (40% and 25% less, respectively), as well as a shallower spectral slope (8% and 4% less, respectively, as measured by a 750-nm/430-nm reflectance ratio) (Fig. 3A, B) (Murchie et al., 2008; Robinson et al., 2008). Group B craters, found in the northern portion of the basin, exhibit similar low-reflectance rims but high-reflectance floors that resemble the interior plains (Fig. 3C, D) (Murchie et al., 2008). Group C consists of craters whose rims and ejecta are comparable in reflectance to the interior plains but have slightly higher reflectance and slightly steeper spectral slope as measured by a 750-nm/430-nm reflectance ratio that is about 2%

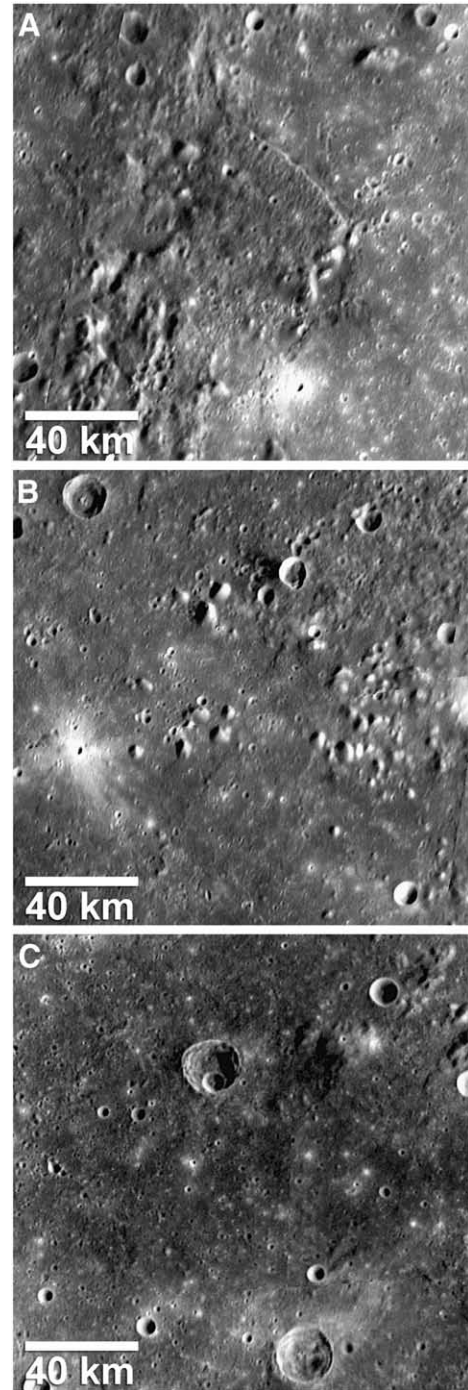


**Fig. 2.** Three of the major units associated with the Caloris basin. (A) Rim massifs are large angular blocks often embayed by interior smooth plains material. (B) Hummocky material is made up of knobs and patches of rolling hills. (C) The circum-Caloris smooth plains are largely featureless (excluding impact craters) except where they are deformed by wrinkle ridges. Locations of panels A–C are shown in Fig. 1A.

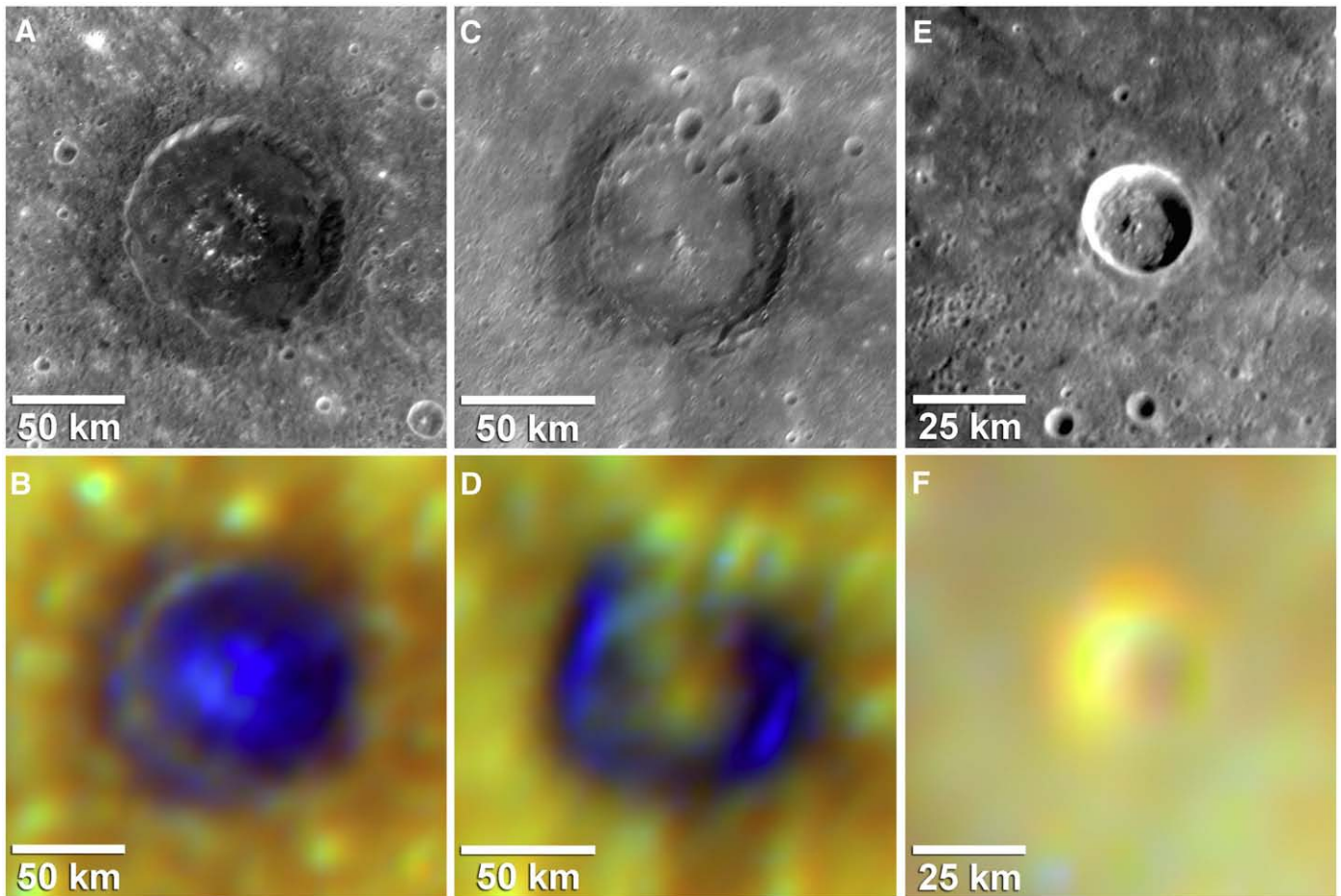


**Fig. 3.** Three impact craters in the interior of the Caloris basin. (A) The gradational contact between the ejecta of the ~100-km-diameter Atget crater and the Caloris basin interior plains material indicates that this group A crater is superimposed on the plains material. (B) The color composite of spectral parameters (inverse of PC2, PC1, and the 430-nm/560-nm reflectance ratio in the red, green, and blue image planes, respectively) shows that the crater walls and floor are similar to dark basin-rim and ejecta materials and distinct from surrounding interior plains material. (C) The sharp contact between surrounding smooth plains material and the impact ejecta indicate that this ~75-km-diameter group B crater formed on the Caloris floor prior to emplacement of the embaying plains. (D) The color composite of spectral parameters shows that the rim and wall of this crater are similar to spectrally dark basin-rim and ejecta materials, whereas material infilling the crater is similar to the surrounding interior plains. (E) A ~20-km-diameter impact crater superposed on Caloris interior smooth plains, with ejecta that are comparable spectrally to the interior plains. The well-preserved ejecta indicate that this group C crater is superposed on the interior plains. (F) The color composite of spectral parameters shows that the material infilling the crater is similar to the surrounding interior plains. The locations of these craters are shown in Fig. 1A.

higher (Fig. 3E, F). In some of the craters, the floors resemble spectrally the rims and ejecta, but in others they are transitional to the low-reflectance floors of group A. Group D consists of fresh craters with bright ejecta rays (Robinson et al., 2008) and reflectances up to tens of percent higher at all wavelengths, as well as a shallower spectral continuum as measured by a 750-nm/430-nm reflectance ratio that is up to 20% lower (Fig. 1).

### 3.3. Diffuse red materials

In isolated patches along the margins of the Caloris basin (Fig. 1) are diffuse red materials comparable in 560-nm reflectance to the brightest parts of the interior plains but displaying a significantly steeper spectral slope with a 750-nm/430-nm reflectance ratio up to 8% higher. These characteristics contrast with those of fresh crater materials whose elevated reflectance is accompanied by a shallower continuum slope. The ovoid patches of red material are 30–100 km in diameter (Murchie et al., 2008; Robinson et al., 2008) and surround irregularly shaped, scalloped-edged, rimless depressions. A kidney-shaped depression ~20 km across at the southwestern margin of the interior plains (Fig. 4) (Head et al., 2008) is surrounded by a bright, smooth, possibly domical red deposit (Fig. 4B), bounded to the northeast by a northwest–southeast-trending wrinkle ridge (Fig. 4A).

Another smaller rimless depression, about 15 km across and surrounded by red deposits, is found along the southern margin of the basin, outside the interior plains (Fig. 4C, D). It is ~60 km beyond the basin rim and flanked by material with the spectral characteristics typical of the basin rim and hummocky material. The morphology of these and other irregularly shaped depressions around Caloris suggests that these landforms are volcanic vents like those observed within lunar maria and on other terrestrial planets (Head et al., 2008; Murchie et al., 2008). The diffuse materials associated with some of the volcanic vents are interpreted as pyroclastic deposits, similar to diffuse pyroclastic deposits on the Moon (Adams et al., 1974; Hawke et al., 1989).

### 3.4. Exterior smooth plains materials

The spectral characteristics of the circum-Caloris exterior smooth plains contrast with those of the basin-interior smooth plains (Fig. 1). The circum-Caloris plains, the largest expanse of LBP yet discovered on Mercury, are ~15% lower in reflectance than the global average (Robinson et al., 2008; Denevi et al., in press). Much of these exterior smooth plains materials are spectrally indistinct from the Caloris rim massifs and hummocky material. The plains materials in the western exterior annulus have basin-radial mottling that extends from the

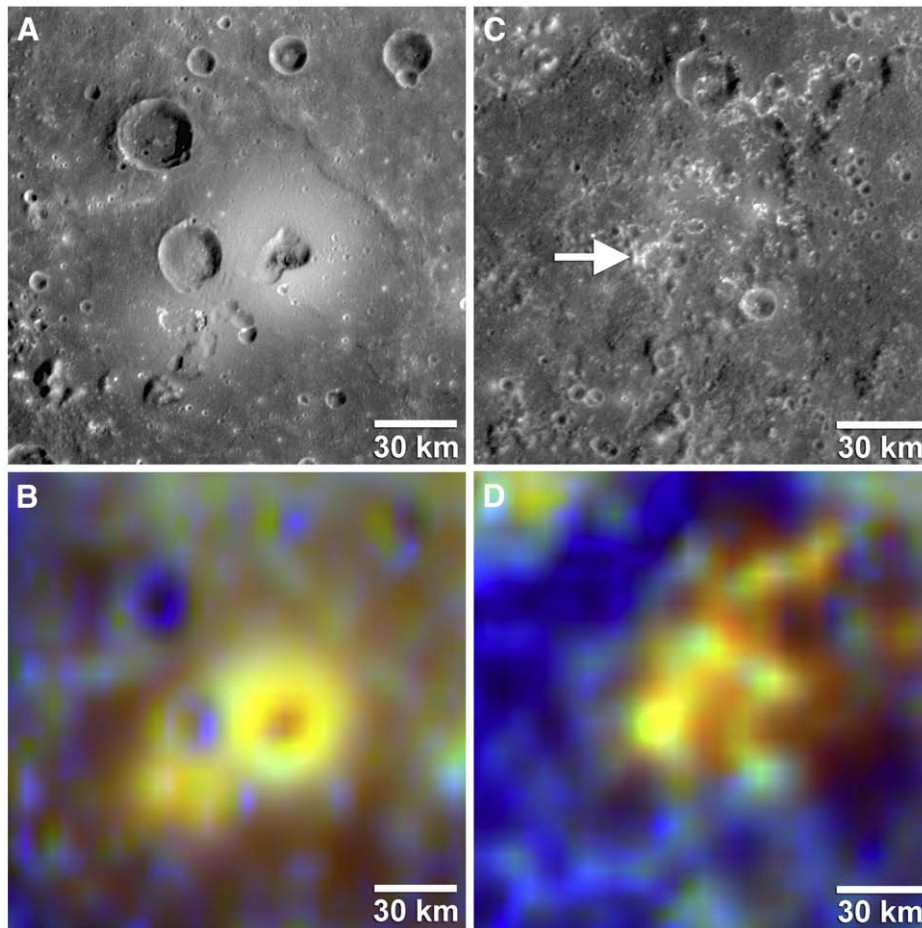


**Fig. 4.** Rimless depressions located near the rim of the Caloris basin. (A) The NAC high-resolution image mosaic shows a rimless, kidney-shaped, depression on the margin of the interior plains surrounded by relatively high-reflectance material. (B) This color composite of the spectral parameters (inverse of PC2, PC1, and the 430-nm/560-nm reflectance ratio in the red, green, and blue image planes, respectively) shows that the rimless depression is surrounded by relatively red material. (C) Another rimless depression, shown in a NAC high-resolution image mosaic (white arrow), is outside the rim of Caloris. (D) The color composite of the spectral parameters shows that this rimless depression is also surrounded by relatively red material. The locations of these features are shown in Fig. 1B.

Caloris basin rim (Fig. 1B) (Robinson et al., 2008, see their fig. 2F). An exception to the dominantly lower-reflectance character of the circum-Caloris exterior smooth plains is Tir Planitia. The southern portions of the Tir smooth plains are spectrally similar to HRP in the Caloris interior plains (Robinson et al., 2008).

#### 4. Tectonic features in basin-interior and basin-exterior plains

##### 4.1. Basin-interior graben

MESSENGER's first flyby of Mercury revealed one of the most remarkable deformational complexes yet observed in an impact basin: Pantheon Fossae, a system of linear graben in the central portion of Caloris (Murchie et al., 2008). Over 230 linear troughs radiate from a zone near the center of the basin (Fig. 5A). Located within this central zone are graben that form polygonal patterns similar to those seen near the basin margin (Fig. 5B). The lengths of the measured graben of Pantheon Fossae range from ~5 km to ~110 km, and widths range from less than 1 km to a maximum of ~8 km.

The impact crater Apollodorus (~40 km diameter) is located within the central zone of Pantheon Fossae (Fig. 5B) and appears visually to be near the center of the graben system. Apollodorus is superposed on the interior smooth plains and, as with other large craters in group A, the rim, walls, and floor of Apollodorus expose underlying LRM (Murchie et al., 2008). The spatial relationship between Pantheon Fossae and Apollodorus (Fig. 5) is of interest

because a crater penetrating smooth plains subjected to extensional pre-stress could significantly influence the location and distribution of normal faults (Freed et al., 2009–this issue). The relation between Apollodorus and Pantheon Fossae, however, is ambiguous. No graben resolved in the currently available images crosscut the rim and floor of Apollodorus. Linear segments of the rim are oriented subparallel to adjacent graben, suggesting structural control of the rim by some preexisting graben. The apparent topographic relief of the graben appears to vanish just outward of the crater rim, suggesting burial by impact ejecta and a formation time for the proximal graben before deposition of ejecta deposits (Murchie et al., 2008). Moreover, Apollodorus is somewhat offset from the center of convergence of the graben. Great circles fit to 743 digitized segments of both proximal and distal graben mostly (>91%) intersect within an approximately circular, 200-km-diameter zone that includes Apollodorus but is centered about 40 km southward of the crater center. All of these observations, however, are from images obtained with less than optimum illumination angle and resolution. Higher-resolution images with better illumination, obtained from orbit, will be needed to ascertain the relationship between Apollodorus and Pantheon Fossae.

A map of tectonic features, combining newly discovered wrinkle ridges and graben in western Caloris with previously mapped features in eastern Caloris, shows that the basin-radial graben of Pantheon Fossae extend to the zone of concentric graben near the basin interior margin (Fig. 6). Apparent gaps in the distribution of the basin-concentric and basin-radial graben west of 170°E are likely in part the

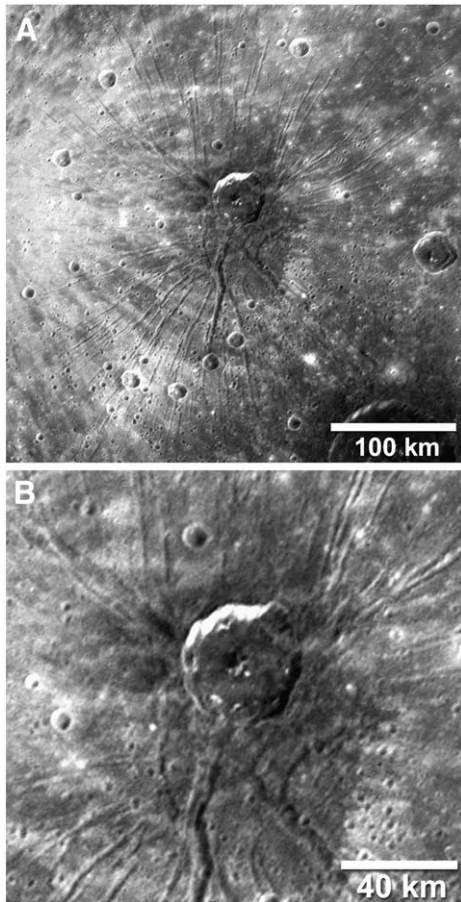


**Fig. 5.** The radial graben complex Pantheon Fossae in the Caloris basin. (A) Linear graben cut the interior plains material and radiate from a zone located near the center of Caloris. The location is shown in Fig. 6B. (B) Some graben form polygonal patterns near the central zone of the radial graben. The ~40-km-diameter impact crater Apollodorus formed near the center of the graben complex.

result of small solar incidence angles (measured from nadir) in the MESSENGER images, which are unfavorable for recognition of low-relief morphologic features. Graben are located throughout the distal portions of the basin interior and record a nearly continuous zone of basin-concentric extension. Radial graben form segments of the giant polygons near the basin margin (Fig. 7). Some graben with basin-radial orientations were observed in Mariner 10 images of eastern Caloris (Strom et al., 1975; Melosh and McKinnon, 1988; Watters et al., 2005), but their association with a central graben complex was not recognized.

The extensional strain expressed by the graben in Caloris can be estimated from displacement-length scaling relations applied to their bounding faults and the lengths of the mapped graben (Scholz and Cowie, 1990; Cowie et al., 1993). The displacement on normal faults in eastern Caloris was estimated by Watters et al. (2005) from Mariner 10 images. For a range of fault plane dip angle  $\theta$  characteristic of normal faults ( $45^\circ$ – $80^\circ$ ), the value of the displacement-to-length ( $D/L$ ) ratio  $\gamma$  obtained by a fit to the  $D/L$  data for these faults ranges from  $\sim 1.9 \times 10^{-3}$  to  $\sim 2.6 \times 10^{-3}$  ( $\sim 2.2 \times 10^{-3}$  at  $\theta = 60^\circ$ ) (Watters et al., 2005). Estimates of  $\gamma$  are complicated by the variability of graben widths and by linkage relations between fault segments (Watters et al., 2005; Watters and Nimmo, in press). The total length of graben in the Caloris basin interior measured thus far from the combined MESSENGER–Mariner 10 data set is  $\sim 15,400$  km. The average areal extensional strain over the entire interior plains, including both inward and outward dipping normal faults, ranges from  $\sim 0.02\%$  to  $\sim 0.13\%$ , depending on the value adopted for  $\theta$  ( $\sim 0.08\%$  for  $\theta = 60^\circ$ ). These values for extensional strain are lower

limits, because the entire population of graben cannot be mapped with the presently available high-Sun images.

#### 4.2. Basin-interior wrinkle ridges

Wrinkle ridges also deform the interior plains of the Caloris basin. The crosscutting relationship between wrinkle ridges and graben in western Caloris is consistent with that observed in the eastern portion of the basin: wrinkle ridges are cut by both basin-radial (Fig. 7) and basin-concentric graben and thus predate the graben. In contrast to the basin-concentric graben, the number of wrinkle ridges per unit area in western Caloris is less than in eastern Caloris (Figs. 6 and 8).

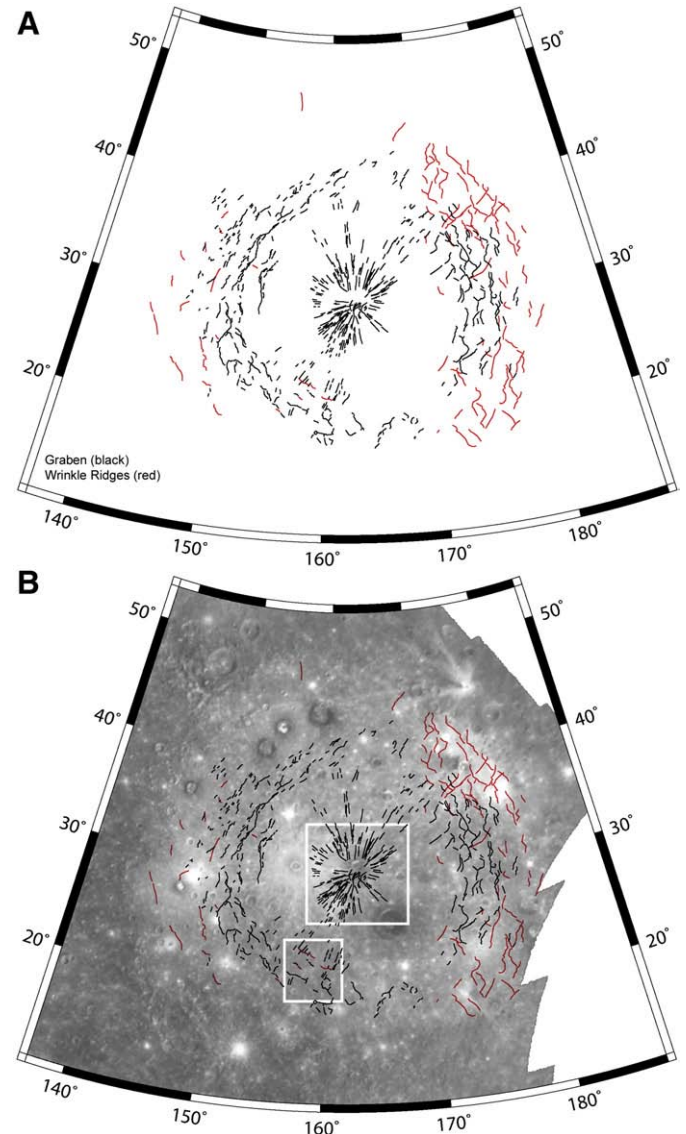


**Fig. 6.** Map of tectonic features in Caloris basin. (A) This map shows 560 graben and 96 wrinkle ridges digitized from MESSENGER and Mariner 10 image mosaics. Gaps in the distribution and differences in the density of tectonic features between western and eastern Caloris may be due, in part, to unfavorable lighting geometry in western Caloris. (B) Here the distributions of graben (black) and wrinkle ridges (red) are overlaid on a NAC high-resolution mosaic. The center of the basin is dominated by the radial graben, which extend outward to a band of concentric and radially oriented graben arrayed in polygonal patterns near the basin margin. Concentric and radially oriented wrinkle ridges near the basin margin coincide with the band of polygonally patterned graben. Buried interior basin rings may have influenced the localization of the wrinkle ridges. The upper white box shows the location of Fig. 5A, and the lower white box shows the location of Fig. 7.

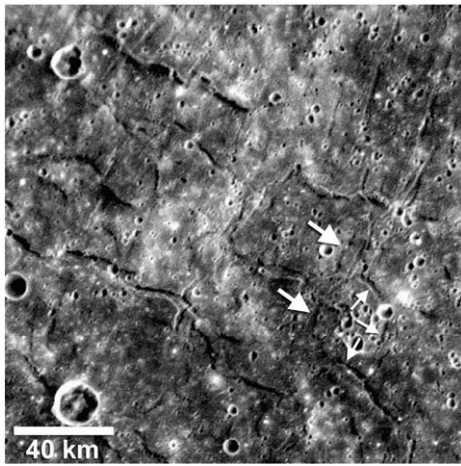


**Fig. 7.** Graben and wrinkle ridges near the southeastern margin of the Caloris basin. Basin-radial graben (large white arrows) that appear to be outward continuations of the central radial graben of Pantheon Fossae make up segments of giant polygons (small white arrows). Basin-concentric wrinkle ridges are crosscut by basin-radial graben. These crosscutting relationships indicate that both basin-concentric and basin-radial graben postdate wrinkle ridges within the Caloris basin. The location is shown in Fig. 6B.

The difference in the distribution of wrinkle ridges (as with the graben) is at least in part an artifact of poor lighting geometry, exacerbated by the low relief and low slopes typical of wrinkle ridges. However, even on the westernmost margin of the Caloris basin where the illumination angles in MESSENGER images is more favorable to identifying subtle topographic features ( $>40^\circ$ ), wrinkle ridges appear to be relatively scarce.

As with the graben, the contractional strain expressed by the wrinkle ridges can be estimated if  $D/L = \gamma$  is known. Watters and Nimmo (in press) estimated the displacement on wrinkle ridges in eastern Caloris imaged by Mariner 10, under the assumptions that the bulk of the strain was due to displacement on thrust faults and that the contribution from folding is minor. For a range of fault plane dip angles characteristic of thrust faults ( $25^\circ$ – $35^\circ$ ), the value of  $\gamma$  obtained is  $\sim 3 \times 10^{-3}$  to  $\sim 4 \times 10^{-3}$  ( $\sim 3.5 \times 10^{-3}$  for  $\theta = 30^\circ$ ) (Watters and Nimmo, in press). The total length of the mapped wrinkle ridges in the interior smooth plains of the Caloris basin is  $\sim 5900$  km. This range of values corresponds to an average contractional strain within the basin of  $\sim 0.06\%$  to  $\sim 0.09\%$ , depending on  $\theta$ , and  $\sim 0.07\%$  for  $\theta = 30^\circ$ . These values for contractional strain also represent a lower limit, because it is likely that the entire population of wrinkle ridges in Caloris has not been mapped.

#### 4.3. Basin-exterior wrinkle ridges

Wrinkle ridges are common in the smooth plains of Tir, Odin, and Suisei Planitiae along the eastern annulus of plains exterior to the Caloris basin (Strom et al., 1975; Melosh and McKinnon, 1988; Watters and Nimmo, in press; Watters et al., 2009-this issue). Few wrinkle ridges, in contrast, have yet been recognized on the exterior smooth plains west of the basin (Fig. 8). As with basin interior features, the distribution of tectonic landforms may be biased by the less than optimal lighting geometry for western Caloris exterior plains. However, NAC images of the western annular plains were obtained with solar incidence angles  $>45^\circ$ , so it is unlikely that a large population of wrinkle ridges has been missed in this area. The contrast in the density of wrinkle ridges between exterior smooth plains to the east and west of Caloris suggests that contractional deformation of the annular plains was not symmetric about the basin.

The orientations of many wrinkle ridges in Tir, Odin, and Suisei Planitiae can be related to the broad-scale geometry of the smooth plains units, which tend to occupy regional topographic lows (Watters

and Nimmo, in press). Topographic data obtained from Earth-based radar show that the smooth plains of northern Tir Planitia are located within a broad, approximately north–south-trending trough lying as much as 1 km below the adjacent intercrater plains (Harmon et al., 1986; Harmon and Campbell, 1988; Watters and Nimmo, in press). Wrinkle ridges on other terrestrial planets are often seen on volcanic plains units within topographic lows (e.g., Hesperia Planum, Mars) (Watters, 1993; Head et al., 2008). The similar settings on Mercury are consistent with a volcanic origin for many smooth plains units and to vertical loading by these plains as a source of subsidence and horizontal contraction. The presence of wrinkle-ridge rings, semi-circular to circular wrinkle ridges that formed over shallowly buried impact craters, provides additional support for a volcanic origin for emplacement and loading (Head et al., 2008; Watters et al., 2009-this issue).

The stress field acting on smooth plains was likely a combination of compressional stresses that accompanied local- and regional-scale loading and compressional stresses associated with global interior cooling and contraction. Loading-induced compressional stresses are strongly influenced by the thickness and distribution of plains materials. A correlation between the orientation of wrinkle ridges and the shape of the lowland plains is observed in Tir, Odin, and Suisei Planitiae (Watters and Nimmo, in press). The comparative paucity of wrinkle ridges on the exterior smooth plains west of Caloris might indicate thinner deposits or a stronger lithosphere at the time of emplacement than for the eastern exterior plains.

## 5. Origin of basin-interior and basin-exterior smooth plains

### 5.1. Basin-interior smooth plains

Evidence supporting a volcanic origin for the Caloris interior plains includes the distinct spectral characteristics of the interior plains compared with the basin rim and superposition relations. Basin rim

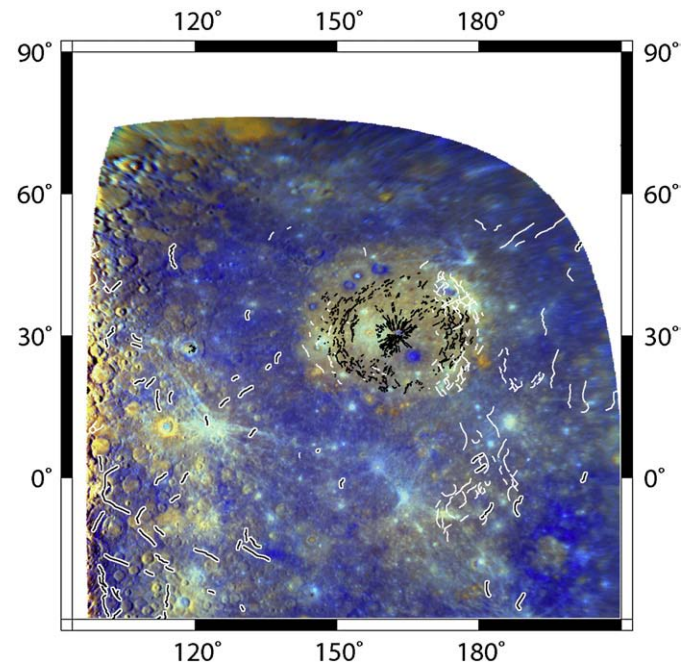


**Fig. 8.** Map of tectonic features in the Caloris basin, circum-Caloris plains, and surroundings. The distributions of wrinkle ridges (white), graben (black), and lobate scarps (black outlined in white) are overlaid on a color composite of spectral parameters (inverse of PC2, PC1, and the 430-nm/560-nm reflectance ratio in the red, green, and blue image planes, respectively). Large numbers of wrinkle ridges east of the basin are on the smooth plains of Tir, Odin, and Suisei Planitiae.

massifs are embayed by interior smooth plains material, consistent with a volcanic emplacement of the plains, but simple embayment relations are not sufficient to rule out an impact origin of the interior plains. The lunar Cayley plains display such embayment relations but were shown by Apollo 16 sampling to be formed of impact breccias (Wilhelms, 1987).

Additional evidence for a volcanic origin of the interior plains comes from embayment relations between the plains material and the spectrally distinct populations of craters. Group B craters have rims of LRM, but their flat interiors spectrally resemble the surrounding interior HRP. The contacts between the interior plains material and crater rims are sharp, suggesting that plains material is superposed on preexisting ejecta (Fig. 3C). We interpret these craters to have formed in or excavated LRM and subsequently to have been embayed, and in some cases flooded, by interior HRP material. Breached rims and interior infilling are also clear evidence for post-impact flooding of craters. The population of group B craters in the basin interior suggests a time interval significantly longer than that expected for the emplacement of Caloris-related impact melts.

In contrast, group A and C craters have spectral and morphologic properties consistent with their formation subsequent to the emplacement of the interior smooth plains (Fig. 3A). Both groups of craters exhibit a gradational contact between their ejecta and plains material, indicating that they are superposed on the interior plains (Fig. 3A, E). The spectral properties of the walls and floors of the relatively large group A craters are consistent with LRM and distinct from surrounding interior plains material (Fig. 3B). The spectral properties of the relatively smaller group C craters are broadly similar to those of the interior HRP and those of possible pyroclastic deposits at the basin margin, except for differences associated with bright crater rays (Fig. 3F). These observations suggest that smaller group C craters excavated only shallower interior HRP materials, whereas larger group A craters excavated more deeply into LRM material. From the observed superposition relations of group A, B, and C craters, the idea that Caloris interior smooth plains consist of impact melt is unlikely. Similar arguments were made by Spudis and Guest (1988) from Mariner 10 images for a volcanic origin for light-colored plains interior to the Tolstoj basin (Robinson and Lucey, 1997; Robinson and Taylor, 2001).

A volcanic origin for Caloris basin interior deposits is indirectly supported by the close proximity of diffuse, relatively red deposits that occur in patches along the margin of the basin (Fig. 1). The associated irregularly shaped, rimless depressions are clearly distinguishable from fresh impact craters (group D craters) with raised rims and bright rays that generally surround very young impacts. The more steeply sloped spectral continuum of the patches contrasts with the bright ejecta of fresh impact craters that have a more shallowly sloped continuum. The scalloped-edged depressions resemble volcanic vents observed in the lunar maria that are often the source for flows and diffuse pyroclastic deposits (Head et al., 2008). The similarity in spectral properties of group C craters and diffuse deposits suggests the possibility that the group C craters may have excavated material resembling the diffuse, red deposits from shallow depths within the interior plains (Murchie et al., 2008).

Although the occurrence of wrinkle ridges in the Caloris interior smooth plains is not diagnostic of volcanic material, their presence constrains the mechanical properties of the deformed material. The morphology of wrinkle ridges is likely related to the presence of layering and to the mechanical contact between layers (Watters, 1991, 2004). In a multi-layered medium, if inter-layer contacts are weak, an upward propagating thrust fault will induce near-surface folding that can produce a wrinkle ridge. If the contacts are strong, in contrast, folding is suppressed and the fault is more likely to break the surface, as in the case of lobate scarps. Volcanic infill is embayed by a succession of flows and perhaps pyroclastic deposits, with intervening regolith layers whose development will depend on the time interval

between successive volcanic events. Impact melt emplaced in a single event, in contrast, is not expected to be strongly stratified, although a sequence of impact breccias separated by well-developed regolith layers might be.

Craters that excavated LRM from beneath or within the interior smooth plains can indicate the depth to LRM source material. For simple craters the depth of excavation is about one-tenth of the diameter of the transient cavity, and the final crater diameter is roughly equal to the transient cavity diameter (Melosh, 1989). For complex craters the final diameter is significantly larger than the transient cavity diameter, and the final diameter must be corrected downward to make a reliable estimate of the depth of excavation. An assumed depth of excavation for complex craters of about 5% of the crater diameter provides a lower bound on the depth to LRM material. From the diameters of smallest craters that expose LRM and the largest craters that do not, the depth to LRM material is estimated to be at least ~1–2 km near the center of the basin. Whether the LRM excavated by the larger craters is basin floor material or is instead material emplaced as magma after basin formation is an open question.

## 5.2. Basin-exterior smooth plains

The contrast in spectral properties between the HRP in the Caloris interior and the LBP in the exterior annulus raises an important question: if the interior and exterior smooth plains share a volcanic origin, why are they spectrally distinct? The only portion of the exterior smooth plains with an HRP spectral signature similar to Caloris interior plains is Tir Planitia. Also, with the exception of Tir Planitia, there is no apparent spatial correlation between the ridged plains and spectral boundaries in the eastern exterior plains (Fig. 8). The densities of impact craters on both the eastern and western exterior plains (Spudis and Guest, 1988; Strom et al., 2008) that include hummocky plains material (Fassett et al., 2009–this issue) show that the exterior plains are younger than the Caloris rim as well as the interior smooth plains, supporting a volcanic origin for the exterior smooth and hummocky plains. A compositional difference in material is the most likely explanation for the spectral contrast between interior and circum-Caloris plains (see Denevi et al., in press). However, as noted in Section 3.4, LBP and the Caloris rim massifs are spectrally similar. Additional multispectral imaging, high-spatial-resolution spectroscopy, and characterization of the impact crater populations of smaller areas well correlated with color and morphological units will be needed to determine the relationship between the Caloris rim and the two expanses of plains material.

## 6. Comparison with lunar maria

### 6.1. Spectral characteristics and composition

Mare basalt contains about 16–20% FeO by weight, compared with <6% FeO in the lunar highlands (Heiken et al., 1991). The Caloris interior smooth plains are higher in reflectance than the lunar maria, suggesting a lower content of low-reflectance minerals containing Fe and Ti (Robinson et al., 2008). In lunar spectra, an absorption band near 1- $\mu\text{m}$  contributed by Fe-bearing silicates is seen in both the maria and highlands and is strongest at young craters because of less obscuration of the absorption band by space weathering. The absence of a 1- $\mu\text{m}$  absorption feature in all areas of Mercury viewed by MESSENGER, including fresh craters, indicates a lower content of Fe-bearing silicates than in the lunar maria and in most lunar highlands (McClintock et al., 2008; Robinson et al., 2008). This inference is consistent with previous Earth-based spectral observations indicating low-FeO silicates (Vilas, 1988; Blewett et al., 1997; Warell et al., 2006).

Superposition relations between impact craters and volcanic fill are well documented on the Moon. For example, on the eastern edge of Mare Imbrium, contacts between mare basalts and the rim of the

crater Archimedes are sharply defined (Fig. 9A). The rim material is spectrally similar to the impact ejecta and adjacent highland material but distinct from the abutting mare units (Fig. 9B), indicating that the mare basalts postdate and are superimposed on preexisting rim and ejecta material. This relationship is similar to that of the group B craters in the interior smooth plains of Caloris (Fig. 3D).

## 6.2. Tectonics

The pattern of central basin-radial graben and outer basin-concentric graben that crosscut wrinkle ridges contrasts sharply with the spatial and temporal distribution of tectonic features within and near lunar maria. In lunar maria, wrinkle ridges occur predominantly in the basin interior, and graben are found near the margins or outside of mascon mare basins (McGill, 1971; Strom, 1972; Maxwell et al., 1975; Golombek, 1979; Solomon and Head, 1980; Watters and Johnson, in press). Moreover, superposition relationships of lunar graben suggest that they are restricted to the older mare basalt units, whereas wrinkle ridges deform both older and younger mare basalt units (Boyce, 1976; Lucchitta and Watkins, 1978; Hiesinger et al., 2003; Watters and Johnson, in press). Crosscutting relationships between wrinkle ridges and graben in Caloris indicate that extension postdates contraction of the floor, in contrast to the sequence of stresses implied for lunar basins.

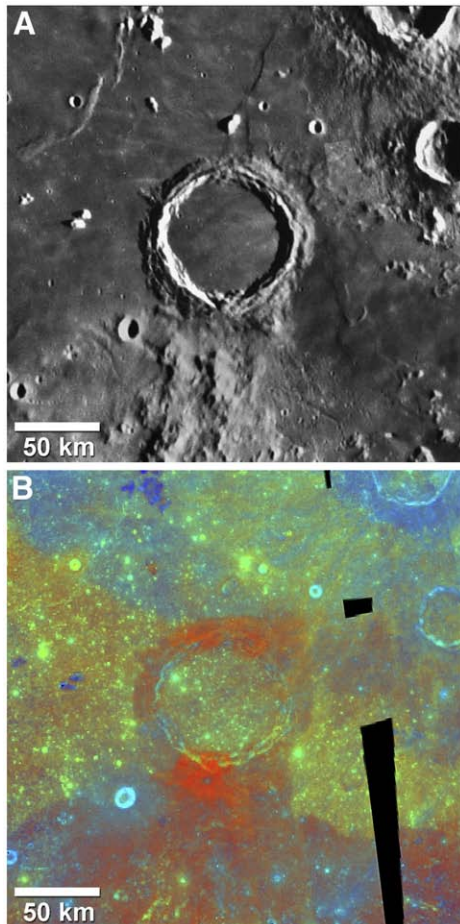


**Fig. 9.** The lunar impact crater Archimedes in Mare Imbrium. (A) Earth-based telescopic image of Archimedes crater obtained from the Consolidated Lunar Atlas shows an embayed crater rim and an interior partially filled by mare deposits. (B) Color-composite Clementine image (red: 750 nm/415 nm; green: 750 nm/950 nm; blue: 415 nm/750 nm) (Pieters et al., 1994) of Archimedes showing contacts between individual flows revealed by their distinct spectral signatures.

The wrinkle ridges in Caloris likely formed in response to subsidence of the interior fill material (Melosh and McKinnon, 1988; Kennedy et al., 2008), possibly aided by lithospheric compressional stress resulting from global interior cooling and contraction (Watters et al., 2005; Watters and Nimmo, in press). On the Moon, the distribution of wrinkle ridges and graben is attributed to loading of the lithosphere by thick sequences of mare basalts that induce lithospheric subsidence and flexure, basin-interior compression, and extension at the basin margins (Phillips et al., 1972; Melosh, 1978; Solomon and Head, 1979, 1980; Freed et al., 2001). The more limited interval of graben formation compared with wrinkle ridge formation on the Moon is thought to result from an accumulation of global compressive stresses induced by interior cooling (Solomon and Head, 1979, 1980). The broad distribution of basin-radial and basin-concentric graben in the interior of Caloris requires an additional deformational process not seen on the Moon.

## 7. Models for tectonic stresses

Two models have been proposed to account for extension in the Caloris interior after an earlier phase of interior subsidence. Melosh and McKinnon (1988) proposed that emplacement of volcanic plains units exterior to the basin caused flexural uplift and extension of the basin interior. For an annular load extending from 650 to 1800 km from the center of the basin and an elastic lithospheric thickness between 75 and 125 km (Melosh and McKinnon, 1988), predicted stresses (Melosh, 1978) are able to account for the distribution of graben within the Caloris basin as viewed by Mariner 10.

The second model, proposed by Watters et al. (2005), invoked lateral flow of the lower crust leading to uplift of the basin interior. For a sufficiently thick (90–140 km) crust, horizontal pressure gradients induced by differences in elevation and crustal thickness between the basin interior and its surroundings could have driven inward flow of the lower crust, even if crustal thickness variations were isostatically compensated after basin formation. The timing and rate of interior uplift would be determined by the crustal thickness, crustal rheology, and mantle heat flux. Under suitable assumptions, including that of a flat-floored initial basin geometry by analogy with inferences from gravity data for lunar mascons (Watters and Konopliv, 2001), the model yields maximum surface extensional stresses at radial distances similar to those of the basin-concentric graben (Watters et al., 2005).

The external loading and lateral flow models were evaluated by finite element analysis by Kennedy et al. (2008) for a range of model assumptions. They found that the distribution of basin-interior graben can be explained by an annular load extending 750–1800 km from the basin center, in agreement with the results of Melosh and McKinnon (1988). Kennedy et al. (2008) also concluded that basin-exterior smooth plains must be thick (>5 km) if extensional stresses from flexural uplift of the basin interior are to exceed residual compressional stresses remaining from interior subsidence, although the required thickness is sensitive to the history of interior infilling and stress relief during ridge formation. Kennedy et al. (2008) confirmed that late-stage lower crustal flow can induce uplift of the basin interior, but the extensional stress pattern from such uplift is not consistent with the distribution of graben in eastern Caloris.

The discovery of the basin-interior radial graben of Pantheon Fossae presents a new constraint for both types of models. Stress models must now account for the transition from a stress state near the basin center where the azimuthal or circumferential stress component is most extensional to one in the outer portions of the basin interior where the radial stress component is most extensional. Two potential mechanisms to accomplish this transition have recently been proposed. In one, the locus of the Pantheon Fossae is a magmatic center, and the radial propagation of vertical dikes of overpressured magma led to graben formation at the tops of the dikes (Head et al.,

2008). The second proposed mechanism is the formation of the Apollodorus crater in a prestressed basin interior (Freed et al., 2009–this issue); impact-induced damage to interior smooth plains material by the cratering event would have caused basin material to move radially outward, leading to a decrease in the radial extensional stress and an increase in the circumferential stress.

The more complete observations of smooth plains deposits exterior to Caloris present new constraints on the hypothesis that Caloris interior uplift is the result of exterior loading. The apparently low density of wrinkle ridges on the western exterior plains, for instance, raises questions regarding the azimuthal symmetry of exterior loading. Topographic, gravity, and further multispectral imaging observations will be needed to improve our understanding of the nature and geometry of interior and exterior plains deposits.

## 8. Conclusions

Images returned from MESSENGER's first flyby of Mercury have revealed the true size of the Caloris basin and the nature of its interior smooth plains. MESSENGER and Mariner 10 data together allow us to reconstruct the complex geologic history of the basin. The basin formed around 3.8 Ga, near the end of the period of heavy impact bombardment (Spudis and Guest, 1988; Strom et al., 2008). MDIS multispectral images show that the interior plains have a spectral signature (HRP) distinct from that of basin rim massifs and the circum-Caloris smooth and hummocky plains (LBP). The measured densities of impact craters show that the smooth and hummocky LBP plains exterior to the Caloris basin are younger than the interior plains (Spudis and Guest, 1988; Strom et al., 2008; Fassett et al., 2009–this issue), indicating that the circum-Caloris plains are volcanic and differ in composition from the interior plains. The origin of the spectral similarity between the rim massifs and the circum-Caloris volcanic plains remains unknown. Both units may have the same composition, or the rim materials may be a physical mixture of an originally heterogeneous target whose spectral signature matches that of the exterior volcanic plains.

Cratering mechanics for large basins are not well understood (Melosh, 1989), but the Caloris event must have sampled material from depths in excess of 40 km, possibly into Mercury's upper mantle. The current location of the most deeply excavated materials is not known, but the rim unit is likely a mixture of materials derived from a range of depths spanning tens of kilometers. At least three mechanisms for mixing can be envisioned to form the rim materials: (1) the bulk of the impacted crust was composed of IP-like materials with numerous intrusions (sills and dikes) having a significant component of LRM; (2) the rim materials are a mixture of lower crustal and upper mantle materials, each with distinct compositions; or (3) the target was composed of a compositionally layered volcanic sequence with a strong component of LRM at the base grading to lesser amounts near the surface. After the formation of the basin and associated ejecta facies, the interior was partially filled with volcanically emplaced materials to form the interior smooth plains. The bulk of the interior plains appears to be HRP because no smaller to medium-size impact craters excavated LRM or LBP from depth. Explosive volcanism occurred contemporaneous with or after the emplacement of the interior plains. The currently identifiable pyroclastic deposits occupy a small area, but because the spectral properties of some impact crater ejecta blankets interior to the Caloris rim show spectral similarity to such deposits, the areal and volumetric significance of explosive volcanism during Caloris basin infilling may have been greater than indicated by surface deposits. Further observations and additional analysis are required to sort out relationships among Caloris units distinguishable on the basis of color and morphology from measurements of crater density and geological mapping of stratigraphic relations, including the acquisition of appropriately illuminated multispectral images and spectral reflectance measurements as well as topographic and gravity information.

Later stages in the history of the Caloris basin are better resolved. Following basin formation and interior volcanic infill, compressional stresses induced by interior loading led to the formation of basin-radial and basin-concentric wrinkle ridges in the interior plains. Following the formation of these wrinkle ridges, lateral crustal flow or basin-exterior loading led to uplift of the basin floor and the formation of graben that were dominantly basin radial near the basin center and basin concentric near the outer margin. Finally, additional impact craters were superposed on the interior plains. Larger impact craters penetrated the interior plains material and excavated LRM from the basin floor or from within early plains units, while smaller craters excavated only interior HRP and perhaps some interbedded pyroclastic deposits.

## Acknowledgments

We thank B. Ray Hawke and Walter S. Kiefer for helpful comments that improved the manuscript. The MESSENGER mission is supported by the NASA Discovery Program through contracts NASW-00002 to the Carnegie Institution of Washington and NAS5-97271 to the Johns Hopkins University Applied Physics Laboratory. This work was also supported by NASA grant NNX07AR60G.

## References

- Adams, J.B., Pieters, C., McCord, T.B., 1974. Orange glass—evidence for regional deposits of pyroclastic origin on the Moon. *Proc. Lunar Sci. Conf.* 5, 171–186.
- Blewett, D.T., Lucey, P.G., Hawke, B.R., 1997. A comparison of mercurian spectral reflectance and spectral quantities with those of the Moon. *Icarus* 129, 217–231.
- Boyce, J.M., 1976. Ages of flow units in the lunar nearside maria based on Lunar Orbiter IV photographs. *Proc. Lunar Planet. Sci. Conf.* 7, 2717–2728.
- Bryan, W.B., 1973. Wrinkle-ridges as deformed surface crust on ponded mare lava. *Proc. Lunar Sci. Conf.* 4, 93–106.
- Cowie, P.A., Scholz, C.H., Edwards, M., Malinverno, A., 1993. Fault strain and seismic coupling on mid-ocean ridges. *J. Geophys. Res.* 98, 17911–17920.
- Denevi, B.W., Robinson, M.S., Solomon, S.C., Murchie, S.L., Blewett, D.T., Domingue, D.L., McCoy, T.J., Ernst, E.M., Head, J.W., Watters, T.R., Chabot, N.L., in press. The evolution of Mercury's crust: a global perspective from MESSENGER. *Science* 324.
- Dzurisin, D., 1978. The tectonic and volcanic history of Mercury as inferred from studies of scarps, ridges, troughs, and other lineaments. *J. Geophys. Res.* 83, 4883–4906.
- Fassett, C.I., Head, J.W., Blewett, D.T., Chapman, C.R., Dickson, J.L., Murchie, S.L., Solomon, S.C., Watters, T.R., 2009. Caloris impact basin: exterior geomorphology, stratigraphy, morphometry, radial sculpture, and smooth plains deposits. *Earth Planet. Sci. Lett.* 285, 297–308 (this issue).
- Freed, A.M., Melosh, H.J., Solomon, S.C., 2001. Tectonics of mascon loading: resolution of the strike-slip faulting paradox. *J. Geophys. Res.* 106, 20603–20620.
- Freed, A.M., Solomon, S.C., Watters, T.R., Phillips, R.J., Zuber, M.T., 2009. Could Pantheon Fossae be the result of the Apollodorus crater-forming impact within the Caloris basin, Mercury? *Earth Planet. Sci. Lett.* 285, 320–327 (this issue).
- Golombek, M.P., 1979. Structural analysis of lunar grabens and the shallow crustal structure of the Moon. *J. Geophys. Res.* 84, 4657–4666.
- Golombek, M.P., Anderson, F.S., Zuber, M.T., 2001. Martian wrinkle ridge topography: evidence for subsurface faults from MOLA. *J. Geophys. Res.* 106, 23811–23821.
- Guest, J.E., Greeley, R., 1983. Geologic map of the Shakespeare quadrangle of Mercury. Map I-1408, Miscellaneous Investigations Series, U. S. Geological Survey, Denver, Colo.
- Harmon, J.K., Campbell, D.B., 1988. Radar observations of Mercury. In: Vilas, F., Chapman, C.R., Matthews, M.S. (Eds.), *Mercury*. University of Arizona Press, Tucson, Ariz., pp. 101–117.
- Harmon, J.K., Campbell, D.B., Bindschadler, K.L., Head, J.W., Shapiro, I.I., 1986. Radar altimetry of Mercury: a preliminary analysis. *J. Geophys. Res.* 91, 385–401.
- Hawke, B.R., Coombs, C.R., Gaddis, L.R., Lucey, P.G., Owensby, P.D., 1989. Remote sensing and geologic studies of localized dark mantle deposits on the Moon. *Proc. Lunar Planet. Sci. Conf.* 19, 255–268.
- Hawkins III, S.E., Boldt, J.D., Darlington, E.H., Espiritu, R., Gold, R.E., Gotwols, B., Grey, M.P., Hash, C.D., Hayes, J.R., Jaskulek, S.E., Kardian, C.J., Keller, M.R., Malaret, E.R., Murchie, S.L., Murphy, P.K., Peacock, K., Prockter, L.M., Reiter, R.A., Robinson, M.S., Schaefer, E.D., Shelton, R.G., Sterner II, R.E., Taylor, H.W., Watters, T.R., Williams, B.D., 2007. The Mercury Dual Imaging System on the MESSENGER spacecraft. *Space Sci. Rev.* 131, 247–338.
- Head, J.W., Murchie, S.L., Prockter, L.M., Robinson, M.S., Solomon, S.C., Strom, R.G., Chapman, C.R., Watters, T.R., McClintock, W.E., Blewett, D.T., Gillis-Davis, J.J., 2008. Volcanism on Mercury: evidence from the first MESSENGER flyby. *Science* 321, 69–72.
- Heiken, G.H., Vaniman, D.T., French, B.M., 1991. *Lunar Sourcebook: A User's Guide to the Moon*. Cambridge University Press, Cambridge, UK. 736 pp.
- Hiesinger, H., Head III, J.W., Wolf, U., Jaumann, R., Neukum, G., 2003. Ages and stratigraphy of mare basalts in Oceanus Procellarum, Mare Nubium, Mare Cognitum, and Mare Insularum. *J. Geophys. Res.* 108, 5065. doi:10.1029/2002JE001985.

- Kennedy, P.J., Freed, A.M., Solomon, S.C., 2008. Mechanisms of faulting in and around Caloris basin, Mercury. *J. Geophys. Res.* 113, E08004. doi:10.1029/2007JE002992.
- Lucchitta, B.K., Watkins, J.A., 1978. Age of graben systems on the Moon. *Proc. Lunar Planet. Sci. Conf.* 9, 3459–3472.
- Maxwell, T.A., Gifford, A.W., 1980. Ridge systems of Caloris: comparison with lunar basins. *Proc. Lunar Planet. Sci. Conf.* 11, 2447–2462.
- Maxwell, T.A., El-Baz, F., Ward, S.W., 1975. Distribution, morphology, and origin of ridges and arches in Mare Serenitatis. *Geol. Soc. Am. Bull.* 86, 1273–1278.
- McClintock, W.E., Izenberg, N.R., Holsclaw, G.M., Blewett, D.T., Domingue, D.L., Head III, J.W., Helbert, J., McCoy, T.J., Murchie, S.L., Robinson, M.S., Solomon, S.C., Sprague, A.L., Vilas, F., 2008. Spectroscopic observations of Mercury's surface reflectance during MESSENGER's first Mercury flyby. *Science* 321, 62–65.
- McGill, G.E., 1971. Attitude of fractures bounding straight and arcuate lunar rilles. *Icarus* 14, 53–58.
- Melosh, H.J., 1978. The tectonics of mascon loading. *Proc. Lunar Planet. Sci. Conf.* 9, 3513–3525.
- Melosh, H.J., 1989. *Impact Cratering: A Geologic Process*. Oxford University Press, New York, 245 pp.
- Melosh, H.J., McKinnon, W.B., 1988. The tectonics of Mercury. In: Vilas, F., Chapman, C.R., Matthews, M.S. (Eds.), *Mercury*. University of Arizona Press, Tucson, Ariz., pp. 374–400.
- Murchie, S.L., Watters, T.R., Robinson, M.S., Head, J.W., Strom, R.G., Chapman, C.R., Solomon, S.C., McClintock, W.E., Prockter, L.M., Domingue, D.L., Blewett, D.T., 2008. Geology of the Caloris basin, Mercury: a new view from MESSENGER. *Science* 321, 73–76.
- Phillips, R.J., Conel, J.E., Abbott, E.A., Sjogren, W.L., Morton, J.B., 1972. Masons: progress toward a unique solution for mass distribution. *J. Geophys. Res.* 77, 7106–7114.
- Pieters, C.M., Staid, M.I., Fischer, E.M., Tompkins, S., He, G., 1994. A sharper view of impact craters from Clementine data. *Science* 266, 1844–1848.
- Plescia, J.B., Golombek, M.P., 1986. Origin of planetary wrinkle ridges based on the study of terrestrial analogs. *Geol. Soc. Am. Bull.* 97, 1289–1299.
- Robinson, M.S., Lucey, P.G., 1997. Recalibrated Mariner 10 color mosaics: implications for mercurian volcanism. *Science* 275, 197–200.
- Robinson, M.S., Taylor, G.J., 2001. Ferrous oxide in Mercury's crust and mantle. *Meteorit. Planet. Sci.* 36, 841–847.
- Robinson, M.S., Murchie, S.L., Blewett, D.T., Domingue, D.L., Hawkins, S.E., Head, J.W., Holsclaw, G.M., McClintock, W.E., McCoy, T.J., McNutt Jr., R.L., Prockter, L.M., Solomon, S.C., Watters, T.R., 2008. Reflectance and color variations on Mercury: indicators of regolith processes and compositional heterogeneity. *Science* 321, 66–69.
- Scholz, C.H., Cowie, P.A., 1990. Determination of total strain from faulting using slip measurements. *Nature* 346, 837–839.
- Schultz, R.A., 2000. Localization of bedding-plane slip and backthrust faults above blind thrust faults: keys to wrinkle ridge structure. *J. Geophys. Res.* 105, 12035–12052.
- Solomon, S.C., Head, J.W., 1979. Vertical movement in mare basins: relation to mare emplacement, basin tectonics, and lunar thermal history. *J. Geophys. Res.* 84, 1667–1682.
- Solomon, S.C., Head, J.W., 1980. Lunar mascon basins: lava filling, tectonics, and evolution of the lithosphere. *Rev. Geophys. Space Phys.* 18, 107–141.
- Solomon, S.C., McNutt Jr., R.L., Watters, T.R., Lawrence, D.J., Feldman, W.C., Head, J.W., Krimigis, S.M., Murchie, S.L., Phillips, R.J., Slavin, J.A., Zuber, M.T., 2008. Return to Mercury: a global perspective on MESSENGER's first Mercury flyby. *Science* 321, 59–62.
- Spudis, P.D., Guest, J.E., 1988. Stratigraphy and geologic history of Mercury. In: Vilas, F., Chapman, C.R., Matthews, M.S. (Eds.), *Mercury*. University of Arizona Press, Tucson, Ariz., pp. 118–164.
- Strom, R.G., 1972. Lunar mare ridges, rings and volcanic ring complexes. *Mod. Geol.* 2, 133–157.
- Strom, R.G., Trask, N.J., Guest, J.E., 1975. Tectonism and volcanism on Mercury. *J. Geophys. Res.* 80, 2478–2507.
- Strom, R.G., Chapman, C.R., Merline, W.J., Solomon, S.C., Head, J.W., 2008. Mercury cratering record viewed from MESSENGER's first flyby. *Science* 321, 79–81.
- Vilas, F., 1988. Surface composition of Mercury from reflectance spectrophotometry. In: Vilas, F., Chapman, C., Matthews, M.S. (Eds.), *Mercury*. University of Arizona Press, Tucson, Ariz., pp. 59–76.
- Warell, J., Sprague, A.L., Emery, J.P., Kozlowski, R.W.H., Long, A., 2006. The 0.7–5.3  $\mu\text{m}$  IR spectra of Mercury and the Moon: evidence for high-Ca clinopyroxene on Mercury. *Icarus* 180, 281–291.
- Watters, T.R., 1988. Wrinkle ridge assemblages on the terrestrial planets. *J. Geophys. Res.* 93, 10236–10254.
- Watters, T.R., 1991. Origin of periodically spaced wrinkle ridges on the Tharsis plateau of Mars. *J. Geophys. Res.* 96, 15599–15616.
- Watters, T.R., 1993. Compressional tectonism on Mars. *J. Geophys. Res.* 98, 17049–17060.
- Watters, T.R., 2004. Elastic dislocation modeling of wrinkle ridges on Mars. *Icarus* 171, 284–294.
- Watters, T.R., Johnson, C.L., in press. Lunar tectonics. In Watters, T.R., Schultz, R.A. (Eds.) *Planetary Tectonics*. Cambridge University Press, Cambridge, UK.
- Watters, T.R., Konopliv, A.S., 2001. The topography and gravity of Mare Serenitatis: implications for subsidence of the mare surface. *Planet. Space Sci.* 49, 743–748.
- Watters, T.R., Nimmo, F., in press. The tectonics of Mercury. In Watters, T.R., Schultz, R.A. (Eds.), *Planetary Tectonics*. Cambridge University Press, Cambridge, UK.
- Watters, T.R., Nimmo, F., Robinson, M.S., 2005. Extensional troughs in the Caloris basin of Mercury: evidence of lateral crustal flow. *Geology* 33, 669–672.
- Watters, T.R., Solomon, S.C., Robinson, M.S., Head, J.W., André, S.L., Hauck II, S.A., Murchie, S.L., 2009. The tectonics of Mercury: the view after MESSENGER's first flyby. *Earth Planet. Sci. Lett.* 285, 283–296 (this issue).
- Wilhelms, D.E., 1976. Mercurian volcanism questioned. *Icarus* 28, 551–558.
- Wilhelms, D.E., 1987. The geologic history of the Moon. *U.S. Geol. Surv. Prof. Paper* 1348, 302 pp.